Vat photopolymerization of fly-like, complex micro-architectures with dissolvable supports

**Authors:** Zhenpeng Xu<sup>a</sup>, Ryan Hensleigh<sup>a</sup>, Nikhil JRK Gerard<sup>bc</sup>, Huachen Cui<sup>a</sup>, Mourad Oudich<sup>bcd</sup>, Wentao Chen<sup>a</sup>, Yun Jing<sup>bc</sup>, and Xiaoyu (Rayne) Zheng<sup>a</sup>

<sup>a</sup>Department of Civil and Environmental Engineering & Department of Mechanical and

Aerospace Engineering, University of California, Los Angeles, CA 90095, USA

<sup>b</sup>Graduate Program in Acoustics, The Pennsylvania State University, University Park,

Pennsylvania 16802, USA

<sup>c</sup>Department of Mechanical and Aerospace Engineering, North Carolina State University, Raleigh,

North Carolina 27695, USA

<sup>d</sup>Institut Jean Lamour, Université de Lorraine, CNRS, Nancy, 54000, France

# \*Corresponding author:

Email address: rayne@seas.ucla.edu (X. Zheng)

Keywords: (photopolymerization, dissolvable support, vibration, metamaterial, magnetoactive

material)

#### **Abstract:**

Recent advances in additive manufacturing of complex geometries enabled the creation of mechanical metamaterials whose exotic properties are based on local control of complex cell geometries. Overhanging and free-hanging features that lack continuous support layers in the previous build volume cannot be directly manufactured, imposing a major design limitation. The resulting metamaterials are limited to single homogenous structural materials, and inherently self-supporting geometries, resulting in constraints of achievable architectures. Realizing arbitrary features is compelling but is inherently limited by process and material support constraints. Here we present a novel light-based additive manufacturing approach capable of printing arbitrary micro-architectures comprising a large array of internally suspended features, large span overhang, and high aspect ratio struts. This method eliminates the need for manual removal of internal supports and enables a suite of multi-functional metamaterials with a range of designed properties, including wide bandgaps for elastic waves at low frequency, switchable wave transmissions, and

products requiring no post support removal. We describe the synthesis and rapid printing of a variety of metamaterials comprising an extensive array of suspended features and demonstrate their metamaterial behaviors. The proposed approach removes scale and unit cell limitations and is capable of achieving embedded features across multiple materials.

#### 1. Introduction

Architected metamaterials with designed three-dimensional architectures exhibit extraordinary structural and multi-functional properties that are not observed in nature and are attractive candidates for applications in energy absorption [1-3], energy transduction [4], fluid control [5], electronic sensors [6, 7], and sound management [8, 9]. While advances in additive manufacturing (AM) techniques, capable of complex and high-resolution features, have made the realization of some of these concepts possible [10-12], most additively manufacturable designs are limited to self-supported 3D architectures that exhibit structurally rigid properties. For example, a structural stiff lattice material typically consists of a network of tetrahedron-octahedron unit cells with inplane struts supported by out-of-plane struts [13] and can be built by most additive manufacturing techniques. A plethora of active and dynamic behaviors, such as negative stiffness [14-17], negative Poisson ratios [18, 19], wide acoustic bandgap [20], as well as stimuli-response behaviors [21-25], however, often exploit overhanging and compliant structural features to generate fast and large displacements via snap-through behaviors [26, 27].

Among additive fabrication approaches, including fused filament fabrication, selective laser sintering, and material jetting, the light-based technique is most suitable for micro-architected metamaterials due to its high resolution (<100 µm) and robust mechanical properties of photopolymers [28-30]. However, only a small fraction of 3D features and architectures can be realized, as most current AM techniques are still limited to self-supporting architectures with a small number of unit cells. AM process joins materials together in a layer-wise fashion. Features that lack support layers cannot be printed, imposing limitations on the design. Therefore, the need for support scaffolding and structures has been well appreciated from the early stages of the AM

techniques development [31-33]. In most cases, light-based printing techniques use support materials made of the same constituents, which later have to be manually removed in post-processing. These limitations make the realization of highly complex metamaterials elusive as internal supports within an extensive array of unit cells cannot be manually removed due to the blockage of internal areas by the complex 3D features. This limitation is becoming increasingly acute as inversely designed 3D topologies aided by topology optimization and artificial intelligence become commonplace [34, 35].

Here, we present a light-based AM approach, multi-material projection stereolithography technique with dissolvable support (mSLAD), for arbitrary complex architectures with a large array of overhanging, fly-like micro-architectures. We achieve this by incorporating a dissolvable material into digital light printing capable of multi-materials. In this process, pillars or scaffolds designed to support overhangs are printed using soluble resin and then selectively dissolved in NaOH solution with sonication applied to accelerate dissolution. This method eliminates geometry constraints of the design for the subsequent manufacturing and can access any arbitrarily complex structure made by various polymers/composites without the need for manual support removal. We designed and printed a suite of 3D metamaterials with a variety of embedded overhanging features, including struts with extreme aspect ratios (>40), branch-like micro-architectures as well as free-standing soft-active materials. We demonstrate several novel structural and functional application possibilities with the proposed approach, including attenuation of structure-borne waves over wide and tailorable frequency ranges with a fraction of weight of its counterpart, as well as selective mode propagation via 3D magnetoactive soft metamaterials.

## 2. System design and methodology

# 2.1. System design and printing process

A generalized schematic of the bottom-up multi-material projection stereolithography (SLA) system [1, 18] is presented in Fig. 1a. To manufacture structures with dissolvable supports, firstly, CAD models are sliced into two different groups of cross-sectional images such that each group represents one material. These two-dimensional slices are subsequently digitized and sent to a UV light engine, which projects images at 405 nm. Then, the spatially patterned UV light is projected through a set of optics and focused on the oxygen-permeable window, which is made of transparent glass coated with polydimethylsiloxane (PDMS). Polymerization initiates at the light-exposed areas, converting it into a solid single layer part and stick to the build platform. A thin oxygen inhibition layer (dead zone) forms above the printing window, prevents solidified resin adhesion. The build platform elevates to replenish resin and repeat the cycle. A material exchanging system is connected to the vat, allowing different resins to be delivered to the vat and solidified. When material change is needed, ethanol is quickly pumped to the chamber, washing off the previous resin trapped inside the printed structure and the resin tank; afterward, a new resin is pumped via the exchanging system to replace the ethanol for printing the following layers. The exchanging process takes 15s to 30s, depending on the resin viscosity. The process was repeated layer by layer, combining multiple materials into a 3D structure. With the current configuration, the light irradiance of the projection system can be up to 7 mW/cm<sup>2</sup> with a lateral printing area of 15x20 mm<sup>2</sup>. The light engine is equipped with a digital micromirror device (DMD) chip of 768x1024 pixels with a projection resolution of 20 µm after projection optics. The layer thickness is set by the vertical motion axis to be 30-50 µm, depending on the cure depth of each resin. After printing,

the sample is cleaned with ethanol and dried using compressed air, followed by UV post-curing  $(\sim 10 \text{ mW/cm}^2)$  for several minutes.

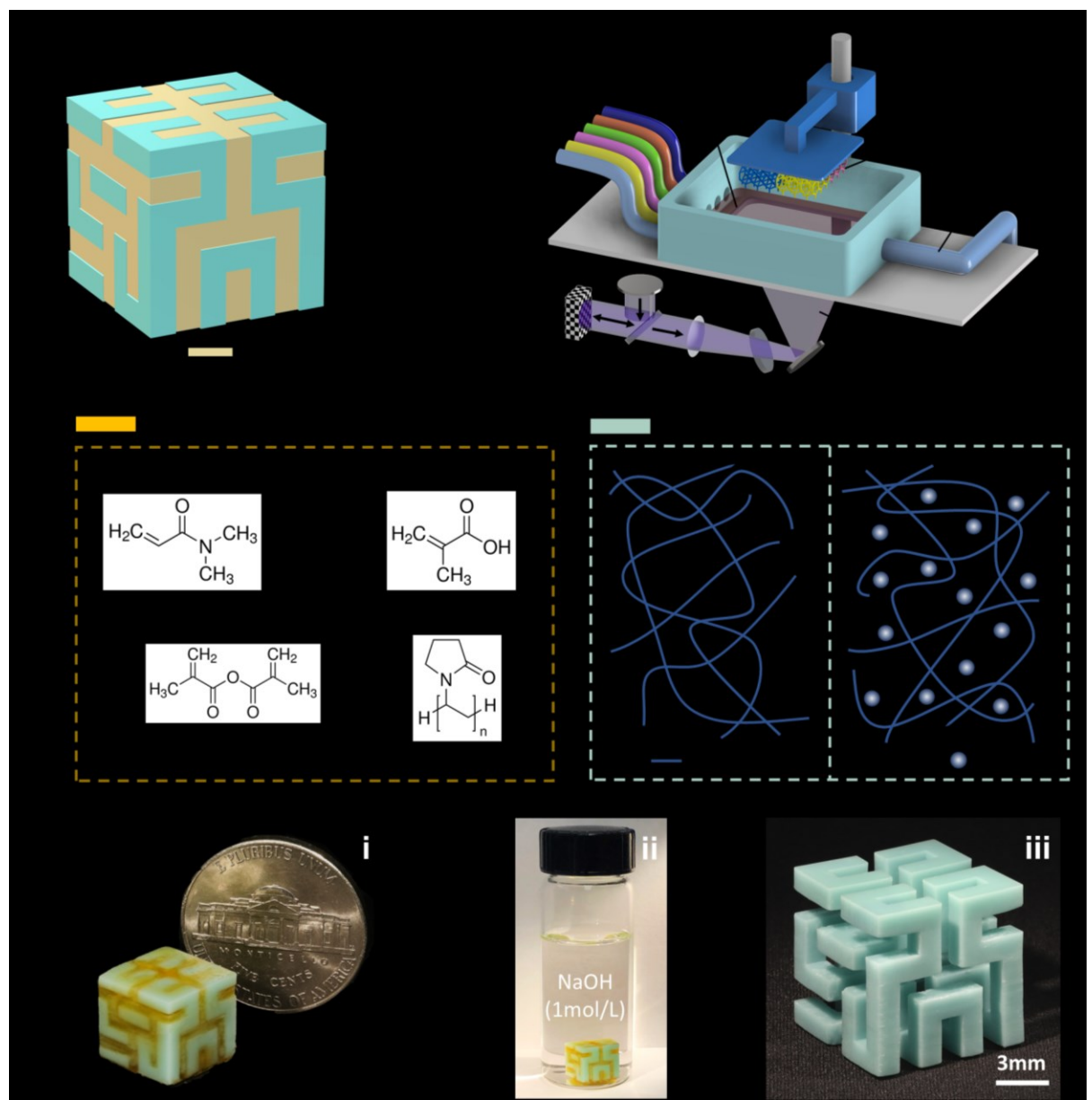


Fig. 1. (a) Schematic of a Hilbert cube with dissimilar constituent material and the multi-material SLA system. (b) Chemical composition of soluble material and schematic of the photopolymer/composite after solidification. (c) Dissolution process of the Hilbert cube: (i) 3D printed Hilbert cube was printed using the multi-material printer. The cyan part is the cube, and the yellow part is dissolvable support. (ii) The cube was then sonicated in NaOH solution. (iii) Hilbert cube after dissolving.

## 2.2. Selective dissolution methodology

Our 3D selective dissolution scheme is based on the arrangement of different materials in a 3D structure and the multi-vat photopolymerization process. To achieve this, we set out to prepare a group of UV-curable resins that will be applied for multi-material printing. As shown in Fig. 1b, we formulate blends of monomers and fillers, a radical initiator, and dye to form a photopolymer resin which is rapidly dissolvable by aqueous base-catalyzed ester hydrolysis to be used as the support material. Base-catalyzed hydrolysis is selected because it has been well known and characterized for 3D printed photopolymer materials. The resins consist of hydrophilic, low molecular weight monomers, which can be rapidly photocured in air, and poly(vinyl pyrrolidone) filler to increase water solubility. High content of monoacrylates makes a low crosslink density network to enhance alkaline solution diffusion in and hydrolyzed polymer out. Through the custom multi-material SLA system, we combine dissolvable resin with typical photopolymer resins, as well as composites, into 3D architectures programmed by the part's digital design.

To demonstrate our scheme, we combined the dissolvable material with a regular commercial photopolymer and printed out a Hilbert cube, which was then soaked in NaOH solution (1 mol/L), along with sonication, to dissolve the support structures (Fig. 1c). Subsequently, the cube was washed in ethanol and dried using compressed air. In this way, a Herbert cube with high feature fidelity (beams width variation: < 5%) and a good surface finish could be formed.

Dissolution time, which ranges from a few minutes to tens of minutes, highly depends on the volume and the surface area of the printed dissolvable material. The smaller the volume and the larger the surface area, the faster the speed. Sonication and temperature are the other two factors

that affect dissolving speed. We tested the dissolving rate of cubes made by dissolvable material under different conditions, and the results reveal that sonication significantly helps the dissolving process, and heating also accelerates the process (Fig. S1). With sonication and heating applied simultaneously, ~80% of the cube (560 mm³) is dissolved in 10 minutes. In practice, heating up to 50°C might damage the desired structure, causing deformation of delicate architecture. Therefore, in this study, the temperature was controlled to be around 30-40°C. Moreover, we find that the heating/etching process won't affect regular polymer's mechanical properties within 6 hours (see Fig. S2).

#### 3. Materials and methods

To demonstrate the methodology's ability to process various polymers/composites for complex architectures, we formulated dissolvable resin, regular polymers, and a photocurable magnetic-responsive soft suspension. These materials have dramatically different properties regarding their inherent mechanical property, processability, and functionality. In this work, a suite of micro-architectures with embedded overhanging features, including elastic and active metamaterials were 3D printed and applied to a few application scenarios as validations of the approach. The following section documents the materials and methods used herein.

# 3.1. Materials and resin preparation

Most materials were purchased from Sigma-Aldrich and used as received: N, N-Dimethylacrylamide, Methacrylic acid, Methacrylic anhydride, Polyvinylpyrrolidone, Phenylbis (2,4,6-trimethylbenzoyl) phosphine oxide (Irg819); Sudan (I); polyethylene glycol diacrylate (PEGDA); Bisphenol A ethoxylate dimethacrylate (BPAEDA); trimethylpropane triacrylate

(TMPTA). For the magnetic resins, Ebecryl 242 and 114 were donated by Allnex. Black iron oxide (Fe<sub>3</sub>O<sub>4</sub>, size of 30 μm) was purchased from Alpha Chemicals, and EPD particles were purchased from Rahn. Cyan resin was purchased from Anycubic.

Dissolvable resin: Acrylic-based photopolymers N, N-Dimethylacrylamide (40 wt%), Methacrylic acid (40 wt%), Methacrylic anhydride (7% wt%), water-soluble filler Polyvinylpyrrolidone (11 wt%), and photoinitiator Irg819 (2% wt%) [36]. PEGDA resin: PEGDA, with 0.05 wt% Sudan (I), and 2 wt% Irg819. BPAEDA-TMPTA: Mixture of BPAEDA and TMPTA (85:15), with 0.05 wt% Sudan (I), and 2 wt% photoinitiator Irg819. Magnetic resin (MAG, 15 vol%): A flexible resin consisting of a mixture of 20 ml Ebecryl 242 and 114 (1:1), 2 wt% EPD, and 2 wt% Irg819 was prepared. 15 g iron oxide particles were combined with the flexible resin in a 50 ml grinding jar and then dispersed with a high-energy ball mill (Retsch) for 50 min.

## 3.2. Measurement of the mechanical properties

To evaluate the mechanical property of the base materials, which will be used as inputs for numerical verification of the experimental results, tensile test samples were prepared using the same printing parameters as the lattices for the mechanical test (per ASTM D3039). The stress-strain response of the samples was captured using an INSTRON 5944 test frame equipped with a 2000 N load cell. A strain rate of 10<sup>-3</sup> 1/s was adopted to ensure that all samples deform quasi-statically. Load-displacement curves were collected by the software linked to the test frame and were converted into engineering strain and stress. Material properties were averaged over the results of three samples per base material. 3 primary materials that were used in this work have a

modulus of 426.9 MPa (PEGDA), 62.3 MPa (BPAEDA-TMPTA), and 6.5 MPa (MAG, 15 vol%). Table S1 lists detailed material properties.

### 3.3. Measurement of wave transmission

A custom measurement platform was built to characterize the dispersion of elastic waves of the metamaterials experimentally. A piezo actuator (PC4QR, ThorLabs) or a piezo film sheet (X2B, TRS technologies) was attached to the bottom plate of the star-shaped lattice/magnetic lattice to produce the input longitudinal excitations. A function generator (SDG 1025, Siglent) and a piezo amplifier (VP7206-24H805, Piezo Master) were used to drive the piezo actuator at a frequency range of 10-10000 Hz for star-shaped lattice and 10-2500 Hz for magnetic lattice (sine wave output). A displacement sensor (LK-H008, Keyence) was used to capture the displacement at 100 kHz sampling frequency. The measured transmission through the sample was then normalized with respect to measurement without the sample. The transmission curves were calculated via the formula,  $T = 20 \log_{10}(A(f)/A_o(f))$ , where T refers to the transmission in dB,  $A_o(f)$  is the amplitude of the actuator and A(f) is the amplitude of the data measured when the sample is in place.

#### 3.4. Band structure and wave transmission simulation

In order to verify the experimentally measured results and understand the underlying wave transmission mechanisms via the trampoline effect enabled by the large overhanging features, numerical simulations were implemented in a commercial finite element software (COMSOL Multiphysics v5.5). For the start-shaped lattice solid, Young's modulus of 62.3 MPa, a density of 1.1 g/cm<sup>3</sup>, and Poisson's ratio of 0.4 were employed. For the magnetic lattice solid, a modulus of 6.5 MPa, density of 1.6 g/cm<sup>3</sup>, Poisson's ratio of 0.4, and a loss factor of 0.75 were employed.

### 4. Results and discussion

In order to demonstrate the applicability of mSLAD and expand the pallet of the processable materials, various micro-architectures and active functional metamaterials were printed and tested: (i) Section 4.1, multiple complex micro-structures comprising many internal supports; (ii) Section 4.2, an ultralight elastic metamaterial that achieves designed vibration attenuation; (iii) Section 4.3, an actively magnetic-responsive metamaterial that made of soft composite. These metamaterials feature complex architectures and resins' processability that precluded their printing using conventional AM techniques.

## 4.1. Realization of various complex micro-architectures

We printed the dissolvable resin into various 3D structures, creating highly complex arbitrary structures with delicate features that were not feasible with manual support removals. As shown in Fig. 2a, a freely moving Voronoi-ball was printed within an enclosed birdcage. Support was added between the cage and ball, which is not accessible for a plier or tweezer restricted by its small-scale and structural geometry. Two intersected hollowed annuls (Fig. 2b) were printed. Fig. 2c shows printed jewelry molds which eliminates post manual support removal and sanding. The reported method leaves almost no residue on the delicate features. Furthermore, this technique could benefit the consumer jewelry industry because any surface that supports are in contact with requires extra post-processing to remove supports manually [37, 38]. Due to the unique property of the dissolvable material, using mSLAD, residues can be avoided on the surface of the printed rings, and many hours could be saved for post-processing. Fig. 2d compares the surface finish of the as-fabricated sample using the conventional support removal method and mSLAD. We observe

that the solution can remove most of the dissolvable material with little residual (see Appendix

Fig. S3 for a quantitive measurement).

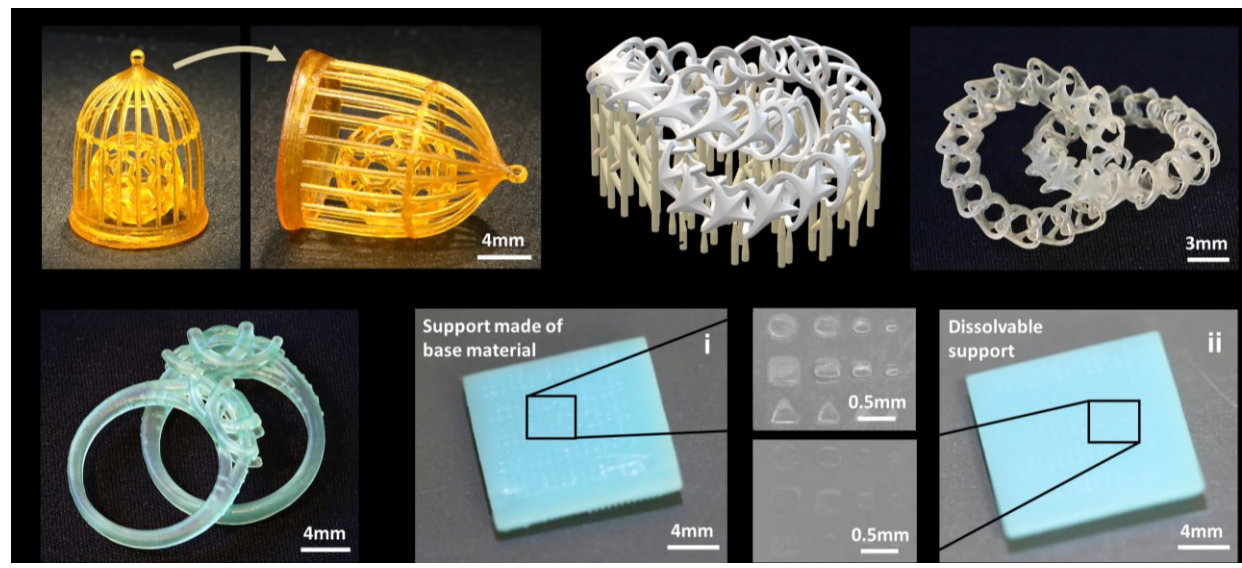


Fig. 2: Fabricated samples. (a) Freely moving Voronoi-ball in a birdcage. (b) Intersected hollowed annulus. (c) 3D printed rings with delicate features. (d) Optical images of structure surface post-fabrication by (i) regular SLA + manual support removal; (ii) mSLAD + Dissolving.

The rapid elimination of support material makes it possible to print complex micro-architected materials with a large array of flying or overhanging features where support removal is extremely challenging in the SLA approach. In Fig. 3, we show a group of as-fabricated lattices with hundreds of internal microscale overhangs, not feasible to be fabricated by other AM techniques. These architectures are typically isotropic, with suspended or fly-like features that will flow away inside liquid once polymerized without solids connecting to the substrate during printing.

Fig. 3a shows a class of isotropic re-entrant metamaterials [39] with internal suspended nodes in all six planes. Thin rods were added in the digital model as dissolvable supports connecting each internal node to the substrate to fix their location during printing. Once printed, these internal rods

were subsequently dissolved, leaving behind isotropic re-entrant lattices with all internal fly-like suspended nodes.

The second category of micro-architectures that are not possible to be printed is embedded large overhangs, which need multiple vertical supports to prevent them from detachment during printing. Fig. 3b shows a type of cubic metamaterial with negative stiffness [14]. The outer cubic frame and the inner re-entrant elements feature large overhangs that are entirely isolated from the substrate. Multiple support beams were designed in and selectively dissolved post-fabrication.

Another class of metamaterials is micro-architectures that are self-supported but with high aspect ratio features and a large inclination angle that, due to gravity and separation force during printing, will significantly deform due to bending-induced deflection. Fig. 3c demonstrates a non-self-supported auxetic metamaterial with a high aspect ratio strut members as high as 40 [40, 41]. Fig. 3d demonstrates the printing of previously unachievable large inclination angle features with soft composite. With an ultimate strength of 0.65 MPa after curing, without support materials at the inclined beams, the soft resin (MAG, 15vol%) tends to fracture and break away from the substrate within a few layers.

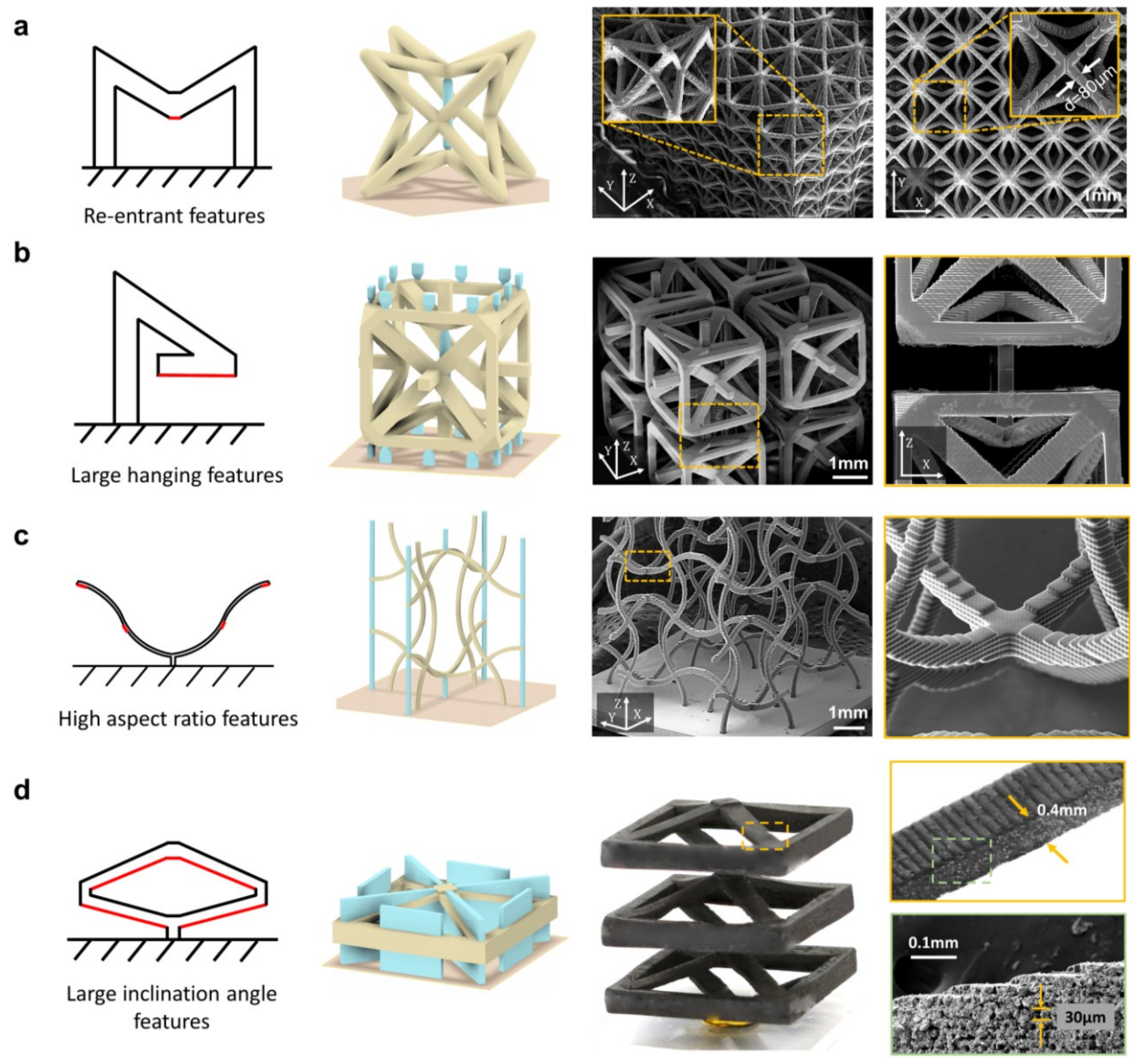


Fig. 3. Classifications of free-standing micro-architectures that require support removal and results of features post mSLAD. The red marks in the 2d schematics denote the overhanging features that need supports. The cyan sections in the 3d schematics refer to the supports. The lattices were printed by mSLAD, and the images were captured using SEM. (a) A re-entrant lattice structure with struts diameter of  $80~\mu m$ . (b) A micro-scale cubic architecture with large overhangs. (c) An auxetic lattice with high aspect ratio struts. (d) A negative stiffness lattice with large inclination angle beams made of soft magnetic composite. The enlarged area shows the high aspect ratio beams that were printed with a layer thickness of  $30~\mu m$ .

### 4.2. Ultralight elastic metamaterial

Incorporating a large number of embedded overhanging and flying features within microarchitectures allows novel metamaterials not achievable by existing approaches. Here we demonstrate a new class of ultralow density elastic micro-architected metamaterials with star-shaped re-entrant topologies that can achieve wide-band omnidirectional vibration attenuation. The high porosity (exceeding 90% void space) of the proposed micro-lattice enables low mass density as low as 0.09 g/cm<sup>3</sup>. The design features a network of low stiffness suspended nodal structures within overhanging micro-unit cells that facilitate a pair of distinct local resonance-based bandgaps at relatively low frequencies.

As shown in Fig. 4a, the star-shaped re-entrant lattice structure composed of isotoxal square stars that are mutually perpendicular to each other in the three orthogonal planes is designed, where over 130 internal supports are needed inside the lattice topology. Each unit cell comprises 30 solid cylindrical rods of the same diameter and intrinsic material. Here, the outer connecting rods and the unique re-entrant structure allow for the existence of multiple omnidirectional local resonance bandgaps for elastic waves and enable complete vibration attenuation over tailorable frequency ranges (For further information, the reader is referenced to the Fig. S4 and previous work [42, 43].). In contrast to metamaterial such as octet truss lattices with all nodes identical and highly connected [13, 44], the unit cell topology of the star-shaped re-entrant metamaterials reveals two distinct nodal structures (node 1 and node 2), as shown in Fig. 4b, where node 1 is suspended in the air. The two distinct types of nodal structures allow for unique local resonance behaviors, giving rise to two distinct bandgaps.

To print such a re-entrant lattice, as shown in Fig. 4a(i), micropillar dissolvable materials were added to connect the nodes of re-entrant struts to support the overhanging edge of each unit cell. Such a design facilitates a shorter fabrication time, and the dissolvable materials are instantly

disassociated during post-processing within several minutes. Fig. 4a(ii) and (iii) show the printed re-entrant micro-lattice with an overall length of 15 mm and a strut radius of 0.2 mm. The existence of two complete bandgaps is first seen in the numerically calculated bandstructure along the different regions of the irreducible Brillouin zone, shown by regions in shaded grey (Fig. 4c).

To experimentally characterize the dispersion of elastic waves, a measurement platform is built, as shown in Fig. 4b, where the lattice is excited by a piezo actuator, and a sensor is placed above the top plate to capture the output displacement amplitude. The lattice in Fig. 4b shows the normalized displacement field map from numerical simulations that the frequency of excitation of the base (here, piezo actuator) lies within the bandgap region. As can be seen here, when an elastic wave at 6 kHz is excited at the bottom plate of the sample, the lattice completely reflects the incident wave; hence, the mechanical vibration does not propagate through more than half a unit cell, leading to high wave attenuation. Fig. 4c shows the calculated bandstructure associated with the lattice and the experimentally measured elastic wave transmission through the sample in the frequency range between 0 and 10 kHz. The experimental curve undergoes sharp decays in transmission for frequencies between 1.90 kHz and 2.25 kHz and from 3.82 kHz to 7.97 kHz, denoting complete wave attenuation in these regions and confirms the existence of the two bandgaps that are observed in the numerically calculated bandstructure shown on the left (shaded grey regions). The presented experimental results agree well with the numerical simulations (Fig. S4), demonstrating two complete bandgaps at low frequency. A slight shift of the bandgaps in the experimental results can be attributed to minor deviations in the intrinsic material's stiffness and the measurement equipment's performance limitations, and this is consistent with the previously

observed bandgaps in the case of a larger sample [43]. Furthermore, via tailoring Young's modulus and feature size of the ligament, a wide frequency range can be achieved, as shown in Fig. 4d.

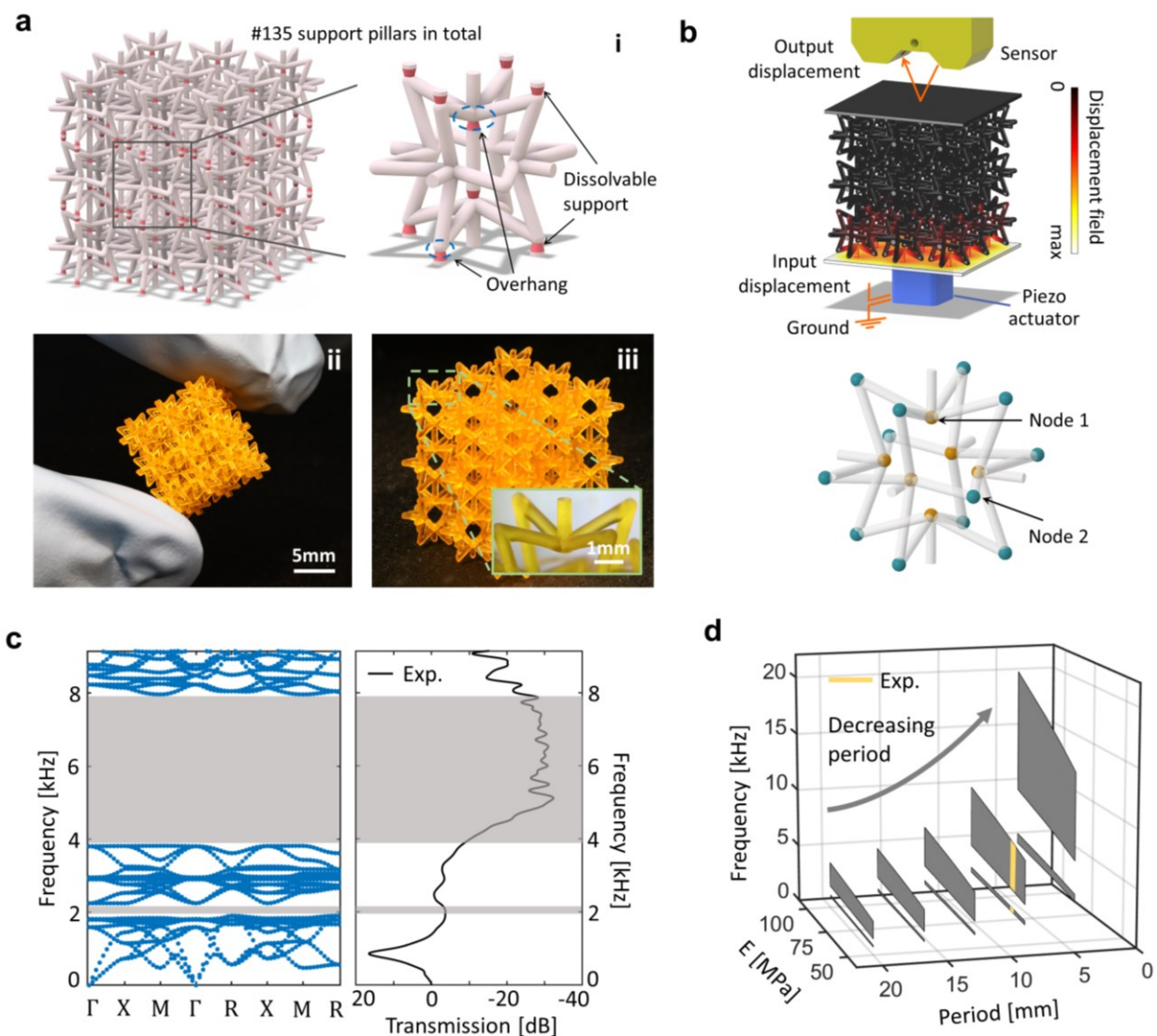


Fig. 4: (a) The star-shaped re-entrant lattice: (i) Designed lattice with 135 internal support pillars, where the circled areas are the overhanging section that needs support, and the pink sections refer to the dissolvable material. (ii)(iii) 3D printed re-entrant lattice (made of BPAEDA-TMTPA) after removal of supports. (b) Schematic of the measurement platform and two different nodes of the star-shaped unit cell. The test sample was printed with side plates using the same material for the testing amenity. The lattice shows the numerical results of the normalized displacement field at a frequency of 6 kHz. (c) Bandstructure of the lattice (left figure) and experimentally measured elastic wave transmission (right figure) through the lattice. The shaded grey regions indicate the bandgaps. (d) Accessing bandgaps that occur at larger frequency ranges by decreasing the structure's period and changing the base materials' stiffness. Period = 8 mm and E = 62 MPa for the tested sample.

# 4.3. Actively tunable magnetic metamaterial

The mSLAD can also be applied to soft multi-functional materials. Here we leverage our fabrication approach to conceive and illustrate magnetically tunable morphing actuators. We design metamaterials that display a negative stiffness (NS) under external axial forces caused by sequential snap-through instabilities [14, 15]. The designed NS structure can exhibit significant shape changes under a remote magnetic field and recover to its original shape upon removing the applied magnetic field. As shown in Fig. 5a, the NS unit cell comprises a cuboid frame and 8 connecting beams with an inclination angle of  $\alpha$ . By tuning the beam aspect ratio  $\lambda = L/h$  and inclination angle, the snap-through response can be tailored accordingly.

To enable the fabrication, we first developed a UV-curable magnetic resin that comprises a mix of soft elastomer and ferrimagnetic particles (see Section 3.1). The cured soft magnetic composite has a stiffness of 6.5 MPa and has a yield stress of 0.35 MPa, which will generate significant deformation and fracture due to large deflection as a result of the low Young's modulus, large inclination angle (77.5°), and high aspect ratio in excess of  $\lambda = 17$  (Fig. S6). Due to the shadowing/blockage of internal areas by the external frames and beams, removing the inner support structures is not feasible with direct SLA. Fig. 5a shows successfully printed magnetic architectures featuring negative stiffness via the snap-through effect.

To enable magnetically actuated structural buckling, we apply a controlled magnetic field B through the lattice (Fig. S7). Fig. 5b demonstrates how the shape of an NS lattice changes with an increasing magnetic field. Unlike a force-induced deformation, Initially, the lattice deforms slightly with the increase of the magnetic field. When the magnetic field is close to the critical

buckling magnetic field (B = 70 mT), a small incremental magnetic force triggers snap-through instability -- the first layer of beams within the lattice snap and are subsequently locked in a new shape. As the magnetic field continues to ramp up, the lattice continues to fold as new layers of architectures reach their critical snap-through thresholds. As a result, the displacement undergoes multiple displacement jumps from one state to another (displaying multiple self-locked shapes, Fig. 5c). Upon switching the magnetic flux to a lower level, the metamaterial will accordingly reverse and lock into its previous state. Reversing the field to zero allows the structure to completely recover to its original unfolded state. As we apply a cyclic magnetic field with a period of 2 s, the lattice morphs back and forth based on the magnetic field amplitude (Movie S1).

These magnetically triggered shape transformations and self-locking can be harnessed to enable controlled elastic wave transmission within designed frequency regimes. We tested the wave transmission properties by exciting the bottom of the lattice with a piezoelectric film sheet with sweep frequencies (0 – 2.5 kHz) and measured their transmission ratio with a laser displacement sensor (Fig. S8), while the lattice shapes are being locked by the magnetic field at the snap-through threshold. The curves in Fig. 5d denote the transmitted wave as a function of frequency for each locked shape (Fig. 5b). These results clearly illustrate that the system enables field-controlled elastic wave transmission. It can be seen that increasing the magnetic field increases the frequency at which the highest transmission occurs, indicated by the different transmission curves corresponding to the magnetic field-triggered lattice shapes. Here, the lattice can be considered as a combination of the spring-mass models, where the 8 connecting beams refer to the spring, and the center cuboid refers to the mass. Each self-locked lattice shapes refer to specific oscillators (spring-mass system). For instance, shape 1 is equivalent to 3 masses coupled with 4 springs, while

shape 3 represents 1 mass coupled with 2 springs. Therefore, such field-responsive metamaterial would possess multiple different transmission frequencies to be selected from a remote magnetic field, which could enable helmets or wearables where desired frequencies are judiciously selected. For example, wave transmissions can be switched "ON" via a discrete set of frequencies or suppressed ("OFF") via other frequencies, shown in the displacement field maps in Fig. 5b and Movie S2.

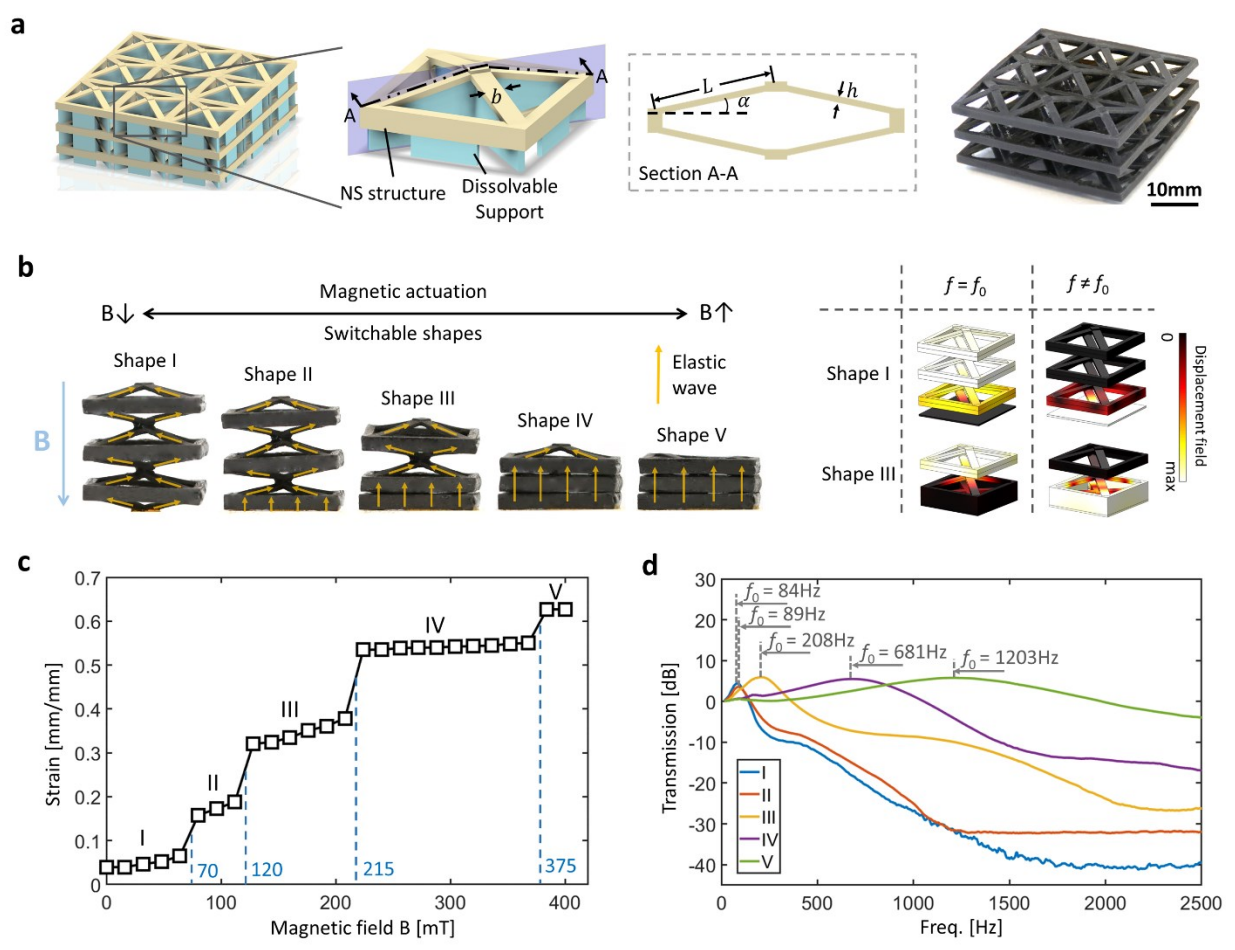


Fig. 5: (a) Negative stiffness magnetic lattice design and printing. (b) The architected negative stiffness structure has configurable shapes under different magnetic fields, resulting in different transmission ratios. Yellow arrow: elastic wave propagation across the structure. The schematics are simulation results of the normalized displacement field for shape 1 and shape 3 at its "ON"  $(f=f_0)$  and "OFF"  $(f \neq f_0)$  status. (c) The effective strain of the lattice as a function of the magnetic field. (d) The measured transmission of elastic waves of the lattice with different shapes. The resonance frequency of the lattice shifts from 84 Hz to 1203 Hz (from shape 1 to shape 5).

### 4.4. Discussion

Comparing the resolution of mSLAD to other multi-material or support-free AM methods compatible with internal support removal and suspended features (Fig. 6), such as fused deposition modeling (FDM) [45-47], selective laser sintering process (SLS) [48-51], and material jetting [52-55], our selective dissolution method enables the fabrication of complex architectures with suspended features at the scale < 100  $\mu$ m (Fig. S9). Additionally, the reported method allows for direct 3D printing of branch-like features and structures with a material Young's Modulus of less than 10 MPa, which is not possible with current stereolithography approaches [56, 57], where the soft materials and overhanging features experience large deflections and are detached from the substrate.

Moving forward, we recognize the limitations of our presented work with respect to scale and printing speed. Specifically, for projection stereolithography, the feature scale is limited to the trade-off between resolution and building area of the light engine. Several strategies can be employed to increase the build area while maintaining resolution, such as moving the translation stage or optics or employing light engines with large pixel numbers. For example, Zheng et al. proposed to use galvanometric mirrors and customized scanning lenses to project the light pattern across a large printing area, enabling microscale features fabricated within a feature size span over four orders of magnitude [44]. Such a technique can be integrated with the mSLAD to increase the build area while keeping a high resolution.

The mSLAD methodology reported herein can also be applied to other multi-material stereolithography techniques. Despite the efficient synchronization between motion stages, pumps,

and image projection sequences, the printing time of the current system can be prolonged to hours when many material exchange processes are involved as a result of the cleansing procedure between a material exchange. Han et al. proposed a multi-material printing system using dynamic fluidic control, which could efficiently switch the printing material and significantly reduced the printing time [58]. This method is also compatible with the dissolvable material and other regular polymers developed for mSLAD.

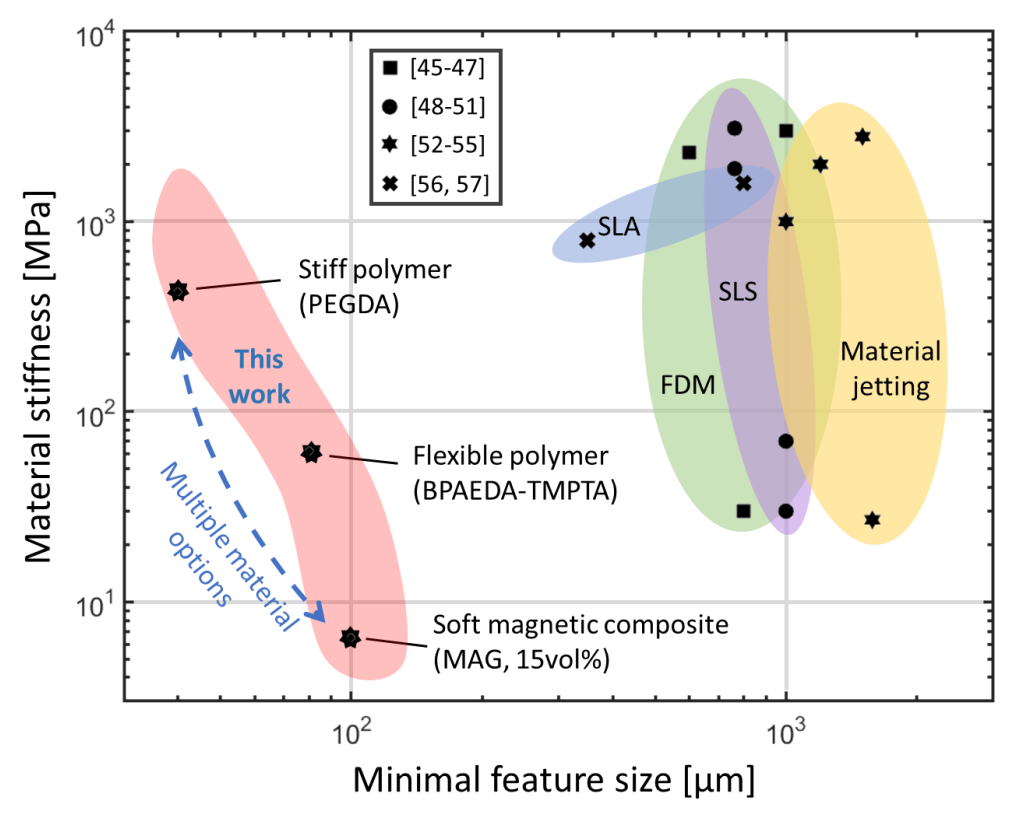


Fig. 6: The accessible feature sizes and range of stiffness enabled by this work and other reported 3D printing techniques capable of printing internal suspended features. mSLAD enables suspended micro-architectures with microscale resolutions and various materials.

## 5. Conclusions

We developed an AM process to create 3D micro-architectures with a large number of free-standing embedded features via dissolving a second phase photopolymer. Using this process, we fabricated complex structures, metamaterials, and soft multi-functional materials with a large array

of fly-like features, large overhangs, and high aspect ratio struts in excess of 40 that are inaccessible by current stereolithography approach. The resolution of this method allows printing features an order of magnitude smaller than techniques including powder bed process, material jetting, and fused deposition modeling. The material process is not limited to polymer; a variety of multi-functional materials, conducting, and ceramics can be incorporated herein. It will have direct implications for streamlined production of jewelry and dental products, metamaterials, bioscaffold, 3D battery architectures, and micro-antennas with arbitrary features and complexity free from manufacturing imposed topology constraints.

## Acknowledgements

The authors would like to thank the US National Science Foundation CAREER award (2048200), US Air Force Office of Scientific Research (FA9550-18-1-0299), US Office of Naval Research (N00014-18-1-2553 and N00014-19-1-2723), US Defense Advanced Research Projects Agency (D20AP00001-02), and the US National Science Foundation (2001677) for their financial support. Y. J. would like to thank startup support from the Pennsylvania State University, USA.

### **Author contributions**

X. Zheng conceived and designed the research. Z. X. carried out the additive manufacturing system setup and performed experiments and measurements. R. H. formulated resin materials. N. J. G., M. O., and Z. X. performed the design and numerical simulations. H. C. and W. C. performed the experiments. Z.X, N. J. G., M. O., Y. J., and X. Z. wrote the paper with contributions from all the authors. X. Z. and Y.J. supervised the project.

#### **Conflict of interest**

The authors declare no conflict of interest.

## **Appendix. Supporting information**

Supplementary data associated with this article can be found in the online version.

## References

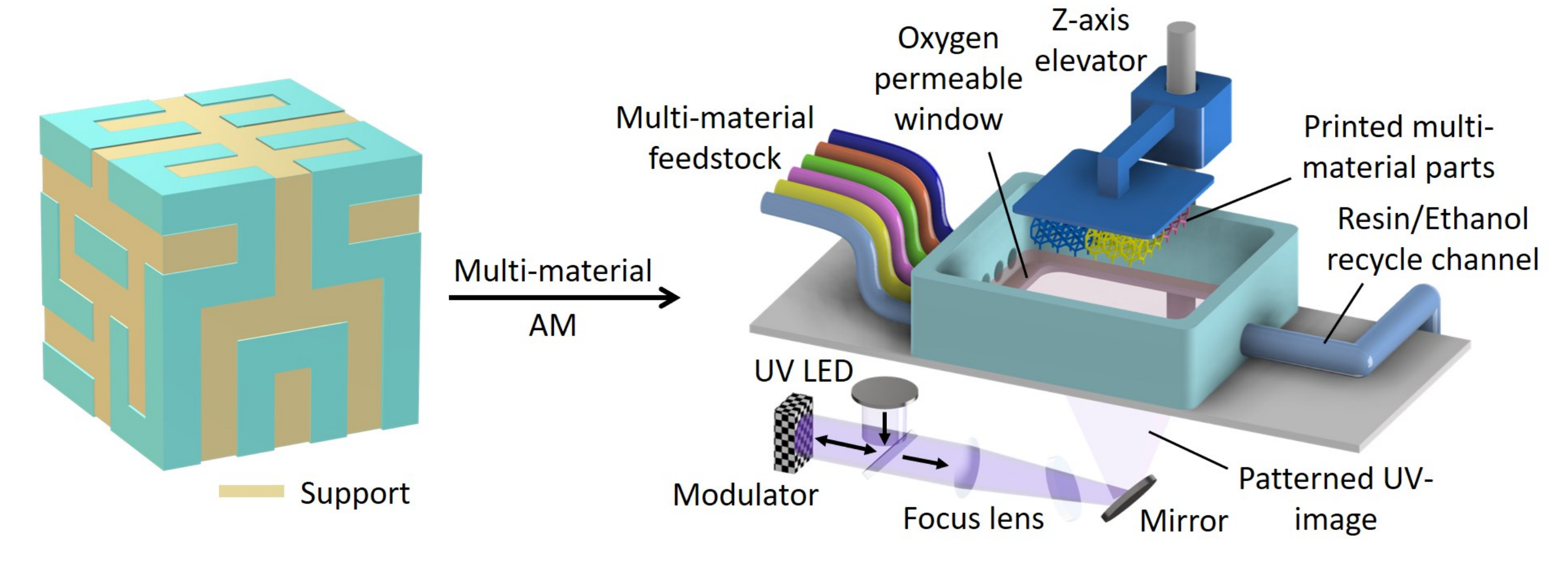
- [1] Z.P. Xu, C.S. Ha, R. Kadam, J. Lindahl, S. Kim, H.F. Wu, V. Kunc, X. Zheng, Additive manufacturing of two-phase lightweight, stiff and high damping carbon fiber reinforced polymer microlattices, Addit Manuf 32 (2020).
- [2] A.G. Izard, L. Valdevit, Magnetoelastic Metamaterials for Energy Dissipation and Wave Filtering, Adv Eng Mater 22(2) (2020).
- [3] M.-T. Hsieh, C.S. Ha, Z. Xu, S. Kim, H.F. Wu, V. Kunc, X. Zheng, Stiff and strong, lightweight bi-material sandwich plate-lattices with enhanced energy absorption, J Mater Res (2021).
- [4] S. Das Mahapatra, P.C. Mohapatra, A.I. Aria, G. Christie, Y.K. Mishra, S. Hofmann, V.K. Thakur, Piezoelectric Materials for Energy Harvesting and Sensing Applications: Roadmap for Future Smart Materials, Adv Sci (2021).
- [5] N.A. Dudukovic, E.J. Fong, H.B. Gemeda, J.R. DeOtte, M.R. Ceron, B.D. Moran, J.T. Davis, S.E. Baker, E.B. Duoss, Cellular fluidics, Nature 595(7865) (2021) 58-+.
- [6] R. Hensleigh, H.C. Cui, Z.P. Xu, J. Massman, D.S. Yao, J. Berrigan, X.Y. Zheng, Charge-programmed three-dimensional printing for multi-material electronic devices, Nature Electronics 3(4) (2020) 216-224.
- [7] D.S. Yao, H.C. Cui, R. Hensleigh, P. Smith, S. Alford, D. Bernero, S. Bush, K. Mann, H.F. Wu, M. Chin-Nieh, G. Youmans, X.Y. Zheng, Achieving the Upper Bound of Piezoelectric Response in Tunable, Wearable 3D Printed Nanocomposites, Adv Funct Mater 29(42) (2019).
- [8] N.J.R.K. Gerard, H.C. Cui, C. Shen, Y.B. Xie, S. Cummer, X.Y. Zheng, Y. Jing, Fabrication and experimental demonstration of a hybrid resonant acoustic gradient index metasurface at 40 kHz, Appl Phys Lett 114(23) (2019).
- [9] Y.F. Zhu, N.J.R.K. Gerard, X.X. Xia, G.C. Stevenson, L.Y. Cao, S.W. Fan, C.M. Spadaccini, Y. Jing, B. Assouar, Systematic Design and Experimental Demonstration of Transmission-Type Multiplexed Acoustic Metaholograms, Adv Funct Mater (2021).
- [10] C.W. Wang, W.W. Ping, Q. Bai, H.C. Cui, R. Hensleigh, R.L. Wang, A.H. Brozena, Z.P. Xu, J.Q. Dai, Y. Pei, C.L. Zheng, G. Pastel, J.L. Gao, X.Z. Wang, H. Wang, J.C. Zhao, B. Yang, X.Y. Zheng, J. Luo, Y.F. Mo, B. Dunn, L.B. Hu, A general method to synthesize and sinter bulk ceramics in seconds, Science 368(6490) (2020) 521-+.
- [11] H.C. Cui, R. Hensleigh, D.S. Yao, D. Maurya, P. Kumar, M.G. Kang, S. Priya, X.Y. Zheng, Three-dimensional printing of piezoelectric materials with designed anisotropy and directional response, Nat Mater 18(3) (2019) 234-+.
- [12] H.C. Cui, R. Hensleigh, H.S. Chen, X.Y. Zheng, Additive Manufacturing and size-dependent mechanical properties of three-dimensional microarchitected, high-temperature ceramic metamaterials, J Mater Res 33(3) (2018) 360-371.
- [13] X.Y. Zheng, H. Lee, T.H. Weisgraber, M. Shusteff, J. DeOtte, E.B. Duoss, J.D. Kuntz, M.M. Biener, Q. Ge, J.A. Jackson, S.O. Kucheyev, N.X. Fang, C.M. Spadaccini, Ultralight, Ultrastiff Mechanical Metamaterials, Science 344(6190) (2014) 1373-1377.
- [14] C.S. Ha, R.S. Lakes, M.E. Plesha, Cubic negative stiffness lattice structure for energy absorption: Numerical and experimental studies, Int J Solids Struct 178 (2019) 127-135.
- [15] C.S. Ha, R.S. Lakes, M.E. Plesha, Design, fabrication, and analysis of lattice exhibiting energy absorption via snap-through behavior, Mater Design 141 (2018) 426-437.
- [16] A. Rafsanjani, A. Akbarzadeh, D. Pasini, Snapping Mechanical Metamaterials under Tension, Adv Mater 27(39) (2015) 5931-5935.
- [17] T. Frenzel, C. Findeisen, M. Kadic, P. Gumbsch, M. Wegener, Tailored Buckling Microlattices as Reusable Light-Weight Shock Absorbers, Adv Mater 28(28) (2016) 5865-+.

- [18] D. Chen, X.Y. Zheng, Multi-material Additive Manufacturing of Metamaterials with Giant, Tailorable Negative Poisson's Ratios, Sci Rep-Uk 8 (2018).
- [19] X.T. Wang, B. Wang, X.W. Li, L. Ma, Mechanical properties of 3D re-entrant auxetic cellular structures, Int J Mech Sci 131 (2017) 396-407.
- [20] S.M. Montgomery, S. Wu, X. Kuang, C.D. Armstrong, C. Zemelka, Q.J. Ze, R.D. Zhang, R.K. Zhao, H.J. Qi, Magneto-Mechanical Metamaterials with Widely Tunable Mechanical Properties and Acoustic Bandgaps, Adv Funct Mater 31(3) (2021).
- [21] T. Frenzel, M. Kadic, M. Wegener, Three-dimensional mechanical metamaterials with a twist, Science 358(6366) (2017) 1072-1074.
- [22] W.W. Wu, D.X. Qi, H.T. Liao, G. Qian, L.C. Geng, Y.H. Niu, J. Liang, Deformation mechanism of innovative 3D chiral metamaterials, Sci Rep-Uk 8 (2018).
- [23] Y.Y. Jiang, Y.N. Li, Novel 3D-Printed Hybrid Auxetic Mechanical Metamaterial with Chirality-Induced Sequential Cell Opening Mechanisms, Adv Eng Mater 20(2) (2018).
- [24] K.H. Yu, N.X. Fang, G.L. Huang, Q.M. Wang, Magnetoactive Acoustic Metamaterials, Adv Mater 30(21) (2018).
- [25] A. Andreu, P.C. Su, J.H. Kim, C.S. Ng, S. Kim, I. Kim, J. Lee, J. Noh, A.S. Subramanian, Y.J. Yoon, 4D printing materials for vat photopolymerization, Addit Manuf 44 (2021).
- [26] S. Wu, W. Hu, Q. Ze, M. Sitti, R. Zhao, Multifunctional magnetic soft composites: a review, Multifunctional materials (2020).
- [27] A.K. Bastola, M. Hossain, A review on magneto-mechanical characterizations of magnetorheological elastomers, Compos Part B-Eng 200 (2020).
- [28] M. Askari, D.A. Hutchins, P.J. Thomas, L. Astolfi, R.L. Watson, M. Abdi, M. Ricci, S. Laureti, L.Z. Nie, S. Freear, R. Wildman, C. Tuck, M. Clarke, E. Woods, A.T. Clare, Additive manufacturing of metamaterials: A review, Addit Manuf 36 (2020).
- [29] D. Behera, S. Chizari, L.A. Shaw, M. Porter, R. Hensleigh, Z.P. Xu, N.K. Roy, L.G. Connolly, X. Zheng, S. Saha, J.B. Hopkins, M.A. Cullinan, Current challenges and potential directions towards precision microscale additive manufacturing-Part II: Laser-based curing, heating, and trapping processes, Precis Eng 68 (2021) 301-318.
- [30] D. Behera, S. Chizari, L.A. Shaw, M. Porter, R. Hensleigh, Z.P. Xu, X.M. Zheng, L.G. Connolly, N.K. Roy, R.M. Panas, S.K. Saha, X.Y. Zheng, J.B. Hopkins, S.C. Chen, M.A. Cullinan, Current challenges and potential directions towards precision microscale additive manufacturing Part IV: Future perspectives, Precis Eng 68 (2021) 197-205.
- [31] J.C. Jiang, X. Xu, J. Stringer, Support Structures for Additive Manufacturing: A Review, J Manuf Mater Proc 2(4) (2018).
- [32] X.J. Chen, J.L. Hu, Q.L. Zhou, C. Politis, Y. Sun, An automatic optimization method for minimizing supporting structures in additive manufacturing, Adv Manuf 8(1) (2020) 49-58.
- [33] J.K. Liu, A.T. Gaynor, S.K. Chen, Z. Kang, K. Suresh, A. Takezawa, L. Li, J. Kato, J.Y. Tang, C.C.L. Wang, L. Cheng, X. Liang, A.C. To, Current and future trends in topology optimization for additive manufacturing, Struct Multidiscip O 57(6) (2018) 2457-2483.
- [34] Z.J. Wu, L. Xia, S.T. Wang, T.L. Shi, Topology optimization of hierarchical lattice structures with substructuring, Comput Method Appl M 345 (2019) 602-617.
- [35] S. Kumar, S.H. Tan, L. Zheng, D.M. Kochmann, Inverse-designed spinodoid metamaterials, Npj Comput Mater 6(1) (2020).
- [36] R. Liska, F. Schwager, C. Maier, R. Cano-Vives, J. Stampfl, Water-soluble photopolymers for rapid prototyping of cellular materials, Journal of Applied Polymer Science 97(6) (2005) 2286-2298.
- [37] Y.L. Yap, W.Y. Yeong, Additive manufacture of fashion and jewellery products: a mini review This paper provides an insight into the future of 3D printing industries for fashion and jewellery products, Virtual Phys Prototy 9(3) (2014) 195-201.

- [38] F. Bertacchini, E. Bilotta, F. Demarco, P. Pantano, C. Scuro, Multi-objective optimization and rapid prototyping for jewelry industry: methodologies and case studies, Int J Adv Manuf Tech 112(9-10) (2021) 2943-2959.
- [39] W.J. Zhang, S.Y. Zhao, R.J. Sun, F. Scarpa, J.W. Wang, In-Plane Mechanical Behavior of a New Star-Re-Entrant Hierarchical Metamaterial, Polymers-Basel 11(7) (2019).
- [40] Y.Y. Chen, T.T. Li, F. Scarpa, L.F. Wang, Lattice Metamaterials with Mechanically Tunable Poisson's Ratio for Vibration Control, Phys Rev Appl 7(2) (2017).
- [41] T. Strek, H. Jopek, K.W. Wojciechowski, The influence of large deformations on mechanical properties of sinusoidal ligament structures, Smart Mater Struct 25(5) (2016).
- [42] N.J. Gerard, M. Oudich, Y. Jing, Omnidirectional elastic wave attenuation via an isotoxal-star-based auxetic micro-lattice, arXiv preprint arXiv:1912.08260 (2019).
- [43] N.J. Gerard, M. Oudich, Z. Xu, D. Yao, H. Cui, C.J. Naify, A. Ikei, C.A. Rohde, X. Zheng, Y. Jing, Three-Dimensional Trampolinelike Behavior in an Ultralight Elastic Metamaterial, Phys Rev Appl 16(2) (2021) 024015.
- [44] X.Y. Zheng, W. Smith, J. Jackson, B. Moran, H.C. Cui, D. Chen, J.C. Ye, N. Fang, N. Rodriguez, T. Weisgraber, C.M. Spadaccini, Multiscale metallic metamaterials, Nat Mater 15(10) (2016) 1100-+.
- [45] S.J. Park, J.E. Lee, J.H. Park, N.K. Lee, M.Y. Lyu, K. Park, M.S. Koo, S.H. Cho, Y. Son, S.H. Park, Enhanced Solubility of the Support in an FDM-Based 3D Printed Structure Using Hydrogen Peroxide under Ultrasonication, Adv Mater Sci Eng 2018 (2018).
- [46] P. Polamaplly, Y.L. Cheng, X.L. Shi, K. Manikandan, X. Zhang, G.E. Kremer, H.T. Qin, 3D printing and characterization of hydroxypropyl methylcellulose and methylcellulose for biodegradable support structures, Polymer 173 (2019) 119-126.
- [47] A. Kumar, S. Verma, J.Y. Jeng, Supportless Lattice Structures for Energy Absorption Fabricated by Fused Deposition Modeling, 3d Print Addit Manuf 7(2) (2020) 85-96.
- [48] Protolabs, Design Guidelines for Selective Laser Sintering (SLS), 2021. <a href="https://www.protolabs.com/">https://www.protolabs.com/</a>. (Accessed 05/31 2021).
- [49] A. Awad, F. Fina, A. Goyanes, S. Gaisford, A.W. Basit, 3D printing: Principles and pharmaceutical applications of selective laser sintering, Int J Pharmaceut 586 (2020).
- [50] T. Xu, W. Shen, X.S. Lin, Y.M. Xie, Mechanical Properties of Additively Manufactured Thermoplastic Polyurethane (TPU) Material Affected by Various Processing Parameters, Polymers-Basel 12(12) (2020).
- [51] H.Z. Wu, O.X. Wang, Y.J. Tian, M.Z. Wang, B. Su, C.Z. Yan, K. Zhou, Y.S. Shi, Selective Laser Sintering-Based 4D Printing of Magnetism-Responsive Grippers, Acs Appl Mater Inter 13(11) (2021) 12679-12688.
- [52] W. Li, A. Ghazanfari, D. McMillen, M.C. Leu, G.E. Hilmas, J. Watts, Fabricating ceramic components with water dissolvable support structures by the Ceramic On-Demand Extrusion process, Cirp Ann-Manuf Techn 66(1) (2017) 225-228.
- [53] V.C.F. Li, X. Kuang, C.M. Hamel, D. Roach, Y.L. Deng, H.J. Qi, Cellulose nanocrystals support material for 3D printing complexly shaped structures via multi-materials-multi-methods printing, Addit Manuf 28 (2019) 14-22.
- [54] Q.Q. Zhang, F. Zhang, S.P. Medarametla, H. Li, C. Zhou, D. Lin, 3D Printing of Graphene Aerogels, Small 12(13) (2016) 1702-1708.
- [55] Y.F. He, F. Zhang, E. Saleh, J. Vaithilingam, N. Aboulkhair, B. Begines, C.J. Tuck, R.J.M. Hague, I.A. Ashcroft, R.D. Wildman, A Tripropylene Glycol Diacrylate-based Polymeric Support Ink for Material Jetting, Addit Manuf 16 (2017) 153-161.
- [56] L. He, F. Fei, W.B. Wang, X. Song, Support-Free Ceramic Stereolithography of Complex Overhanging Structures Based on an Elasto-viscoplastic Suspension Feedstock, Acs Appl Mater Inter 11(20) (2019) 18849-18857.
- [57] J. Jin, Y. Chen, Highly removable water support for Stereolithography, Journal of Manufacturing Processes 28 (2017) 541-549.

[58] D. Han, C. Yang, N.X. Fang, H. Lee, Rapid multi-material 3D printing with projection microstereolithography using dynamic fluidic control, Addit Manuf 27 (2019) 606-615.





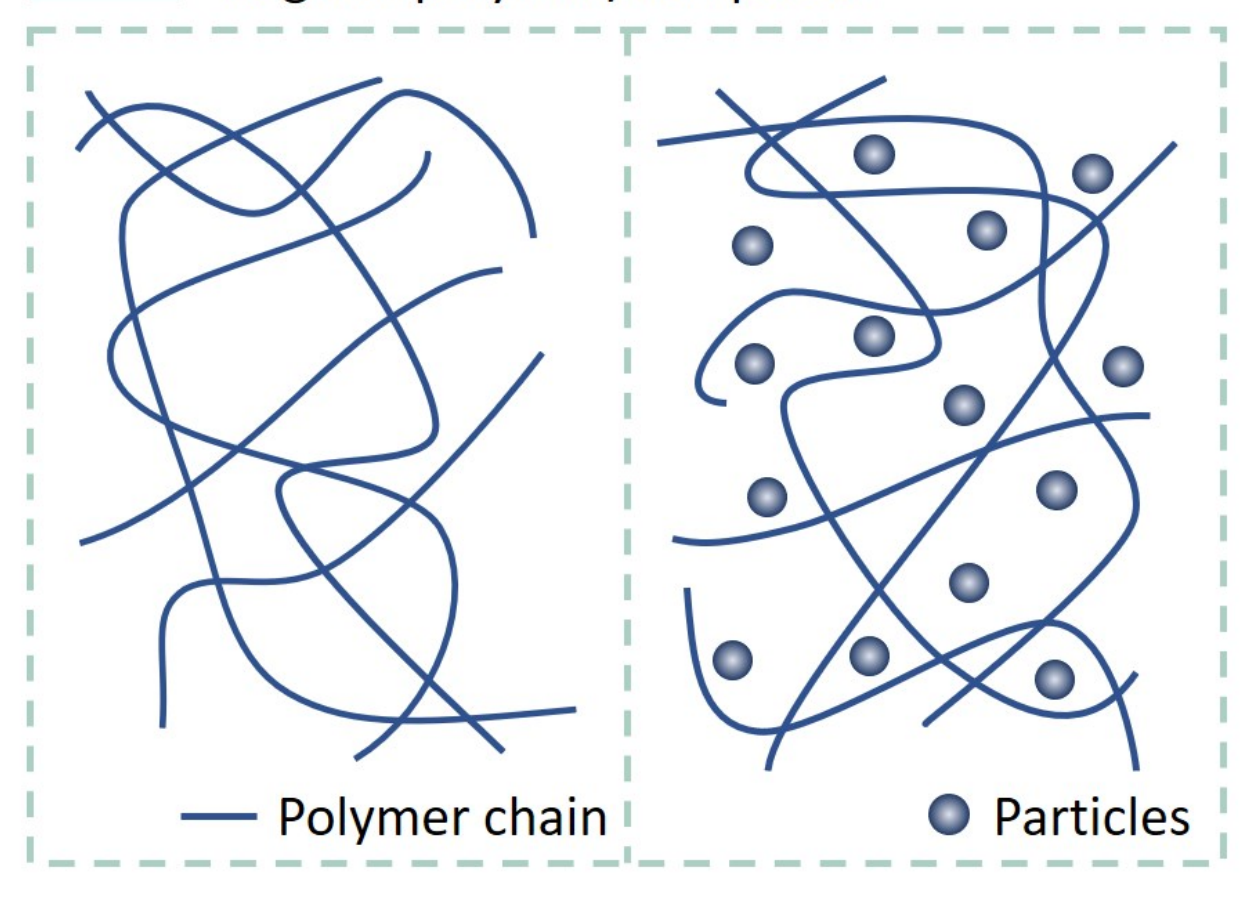
b

Dissolvable material

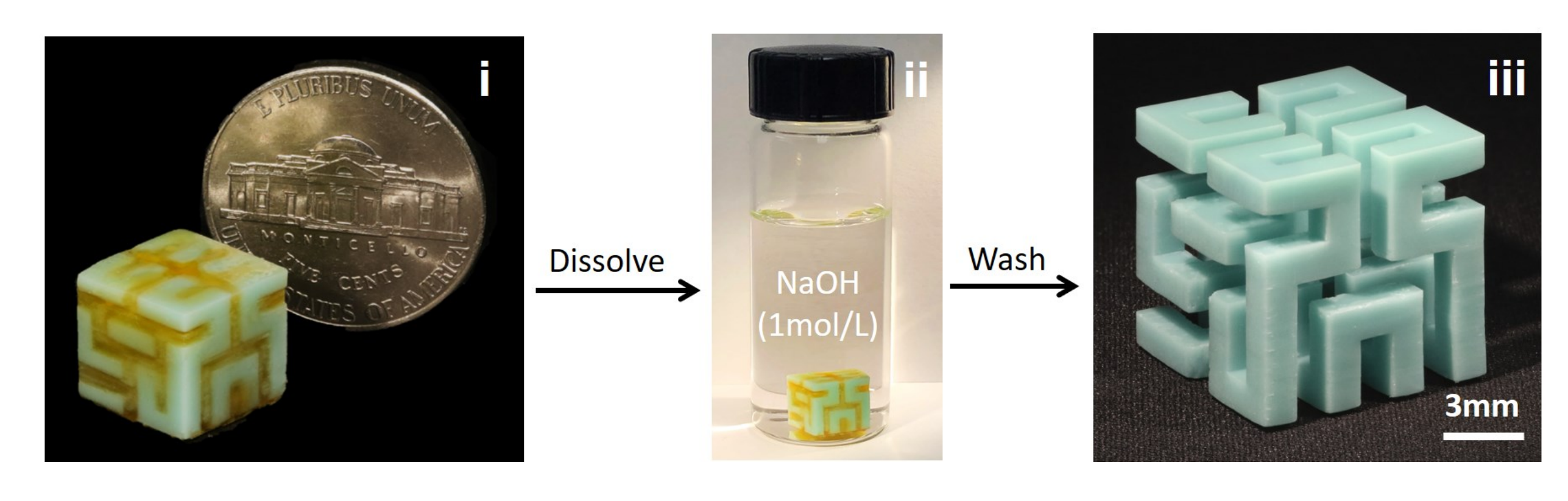
N,N-Dimethylacrylamide Methacrylic acid  $H_2C$  N  $CH_3$   $CH_3$   $CH_3$   $CH_3$   $CH_3$   $CH_3$   $CH_3$   $CH_3$   $CH_3$   $CH_4$   $CH_5$   $CH_5$ 

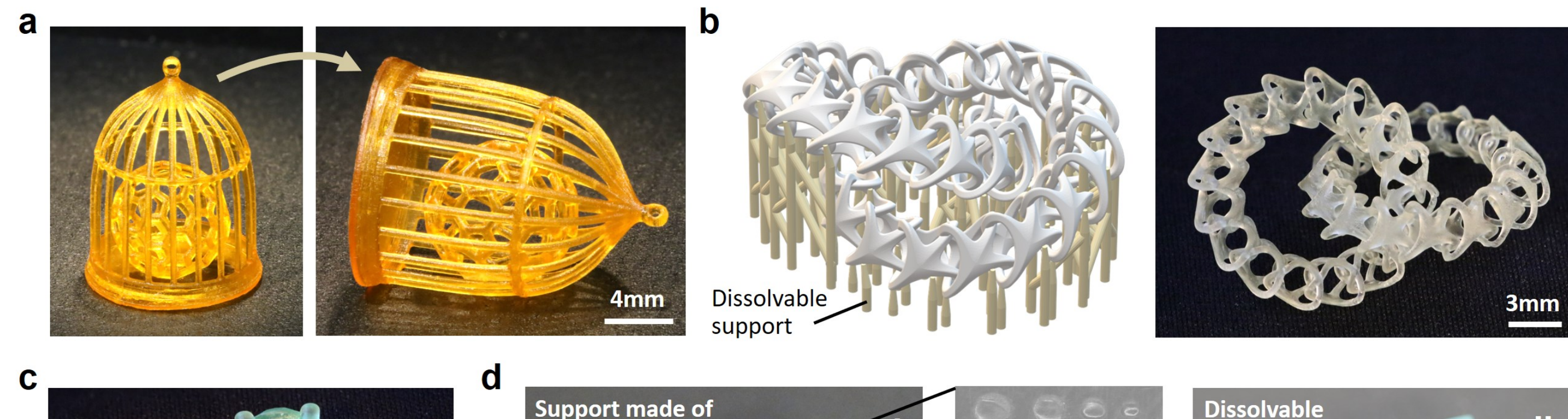
+ Photo-initiator + UV blocker

Regular polymer/composite

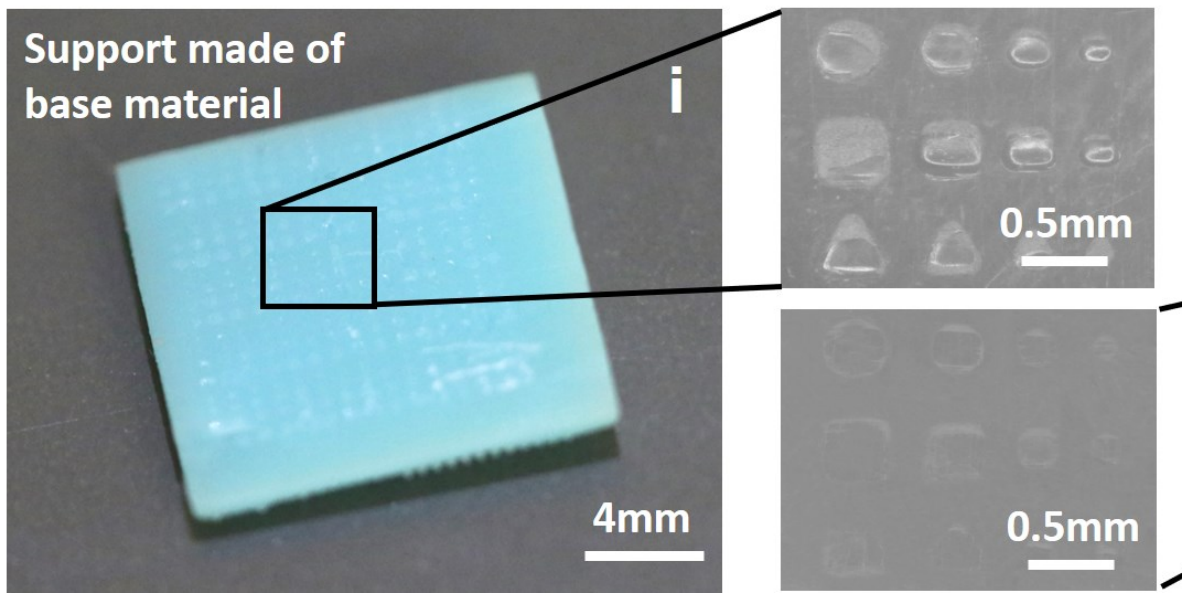


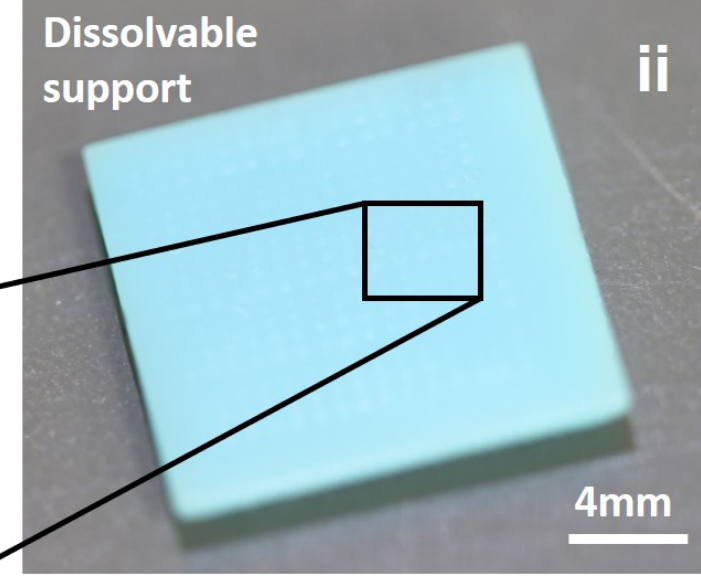
C



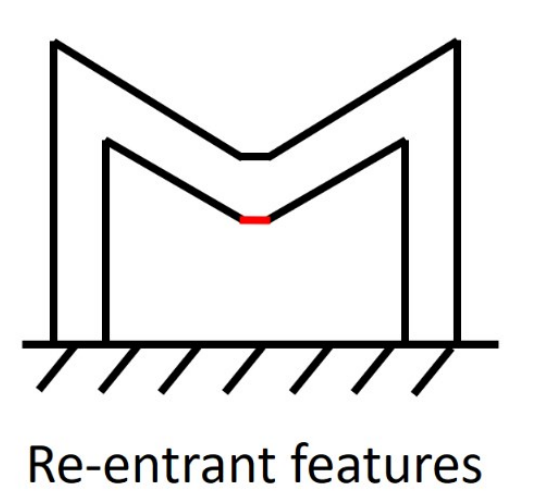


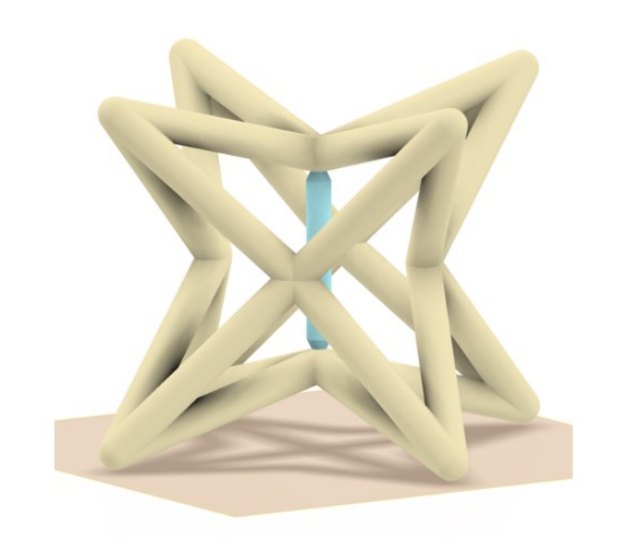


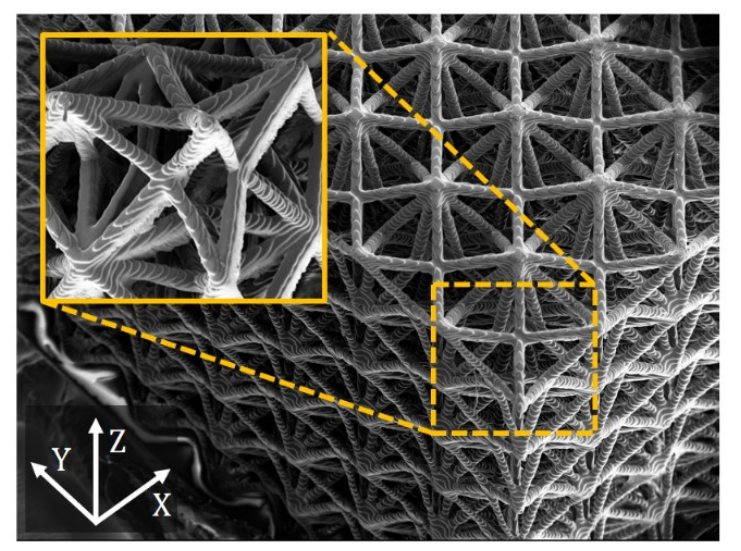


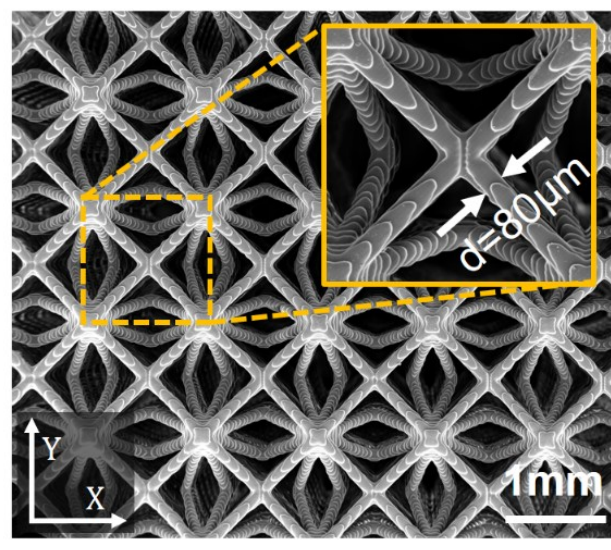


a

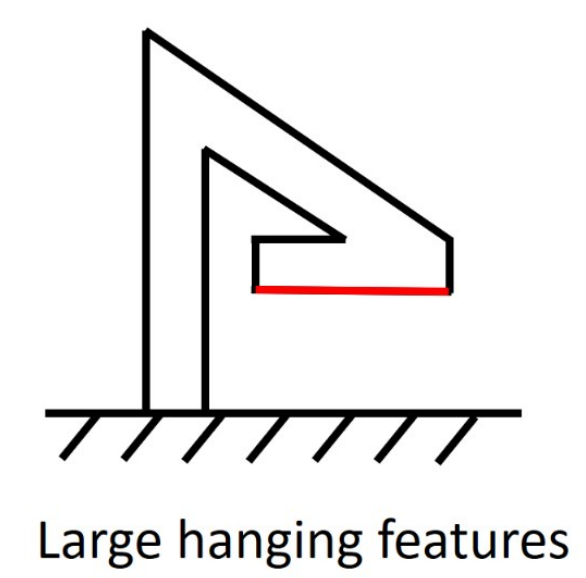


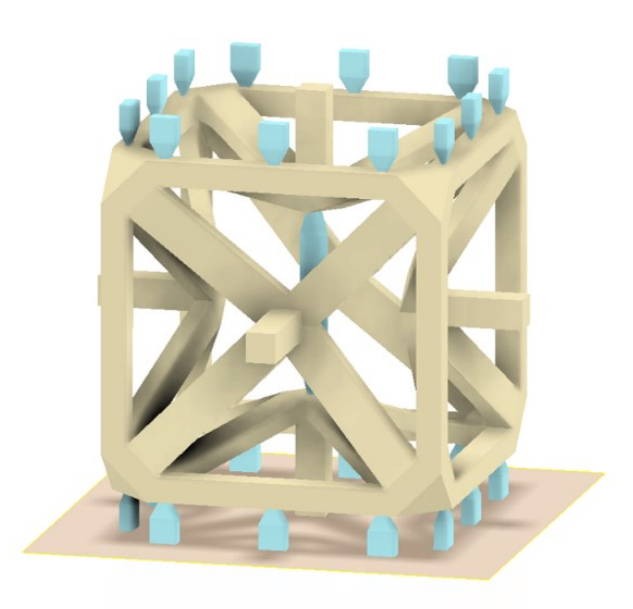


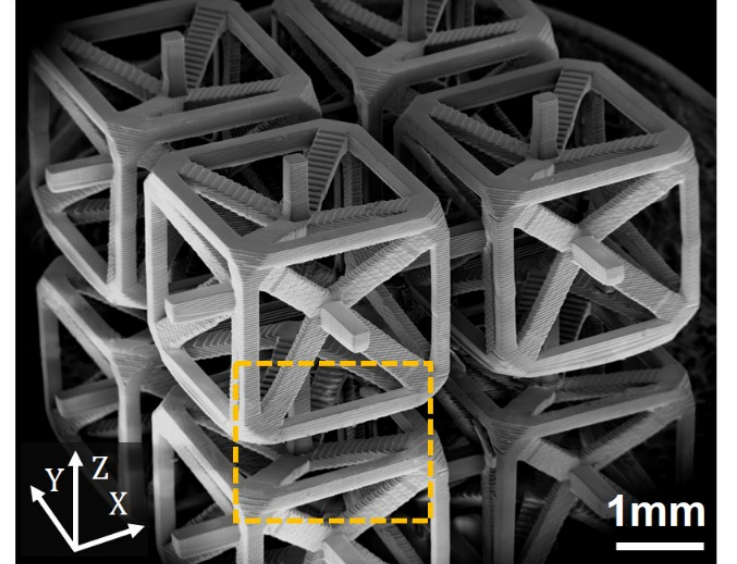


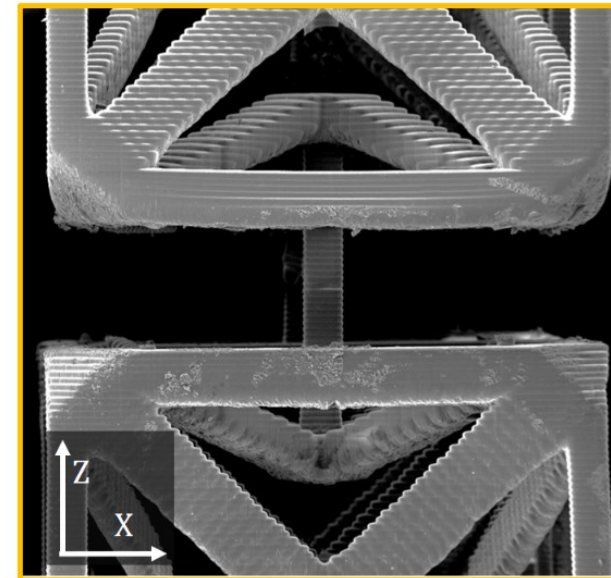


b

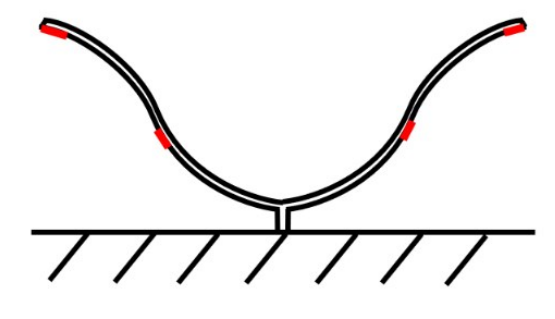


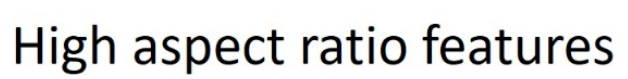


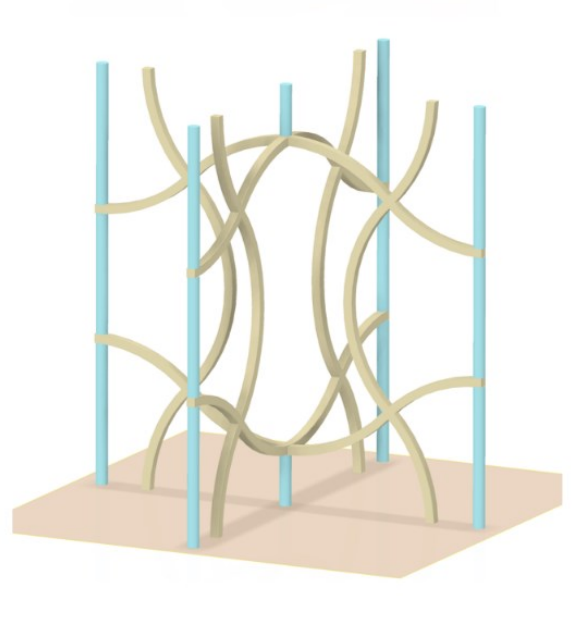


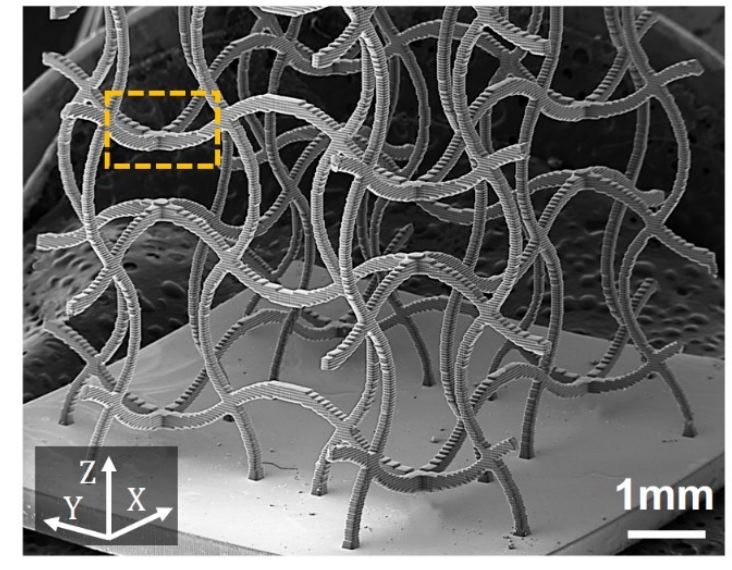


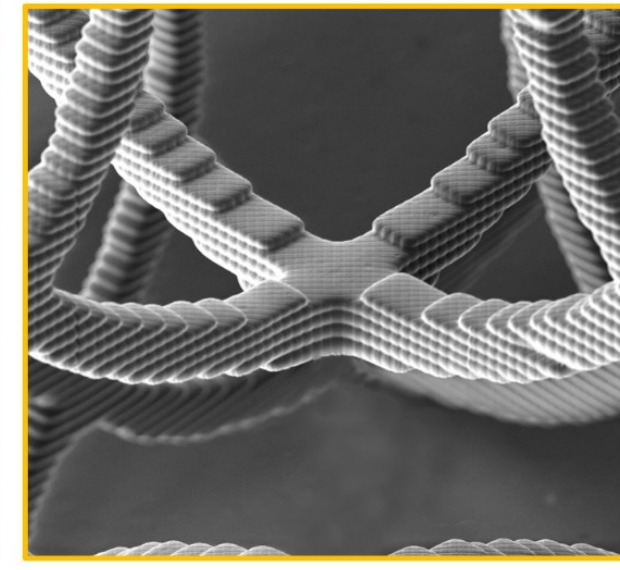
C



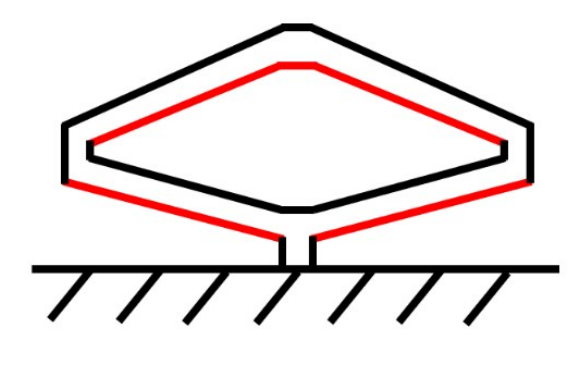








d



Large inclination angle features





